Frequency fluctuations in silicon nanoresonators
Supplementary Information

Marc Sansa, Eric Sage, Elizabeth C. Bullard, Marc Gély, Thomas Alava, Eric Colinet, Akshay K. Naik, Luis Guillermo Villanueva, Laurent Duraffourg, Michael L. Roukes, Guillaume Jourdan, Sébastien Hentz

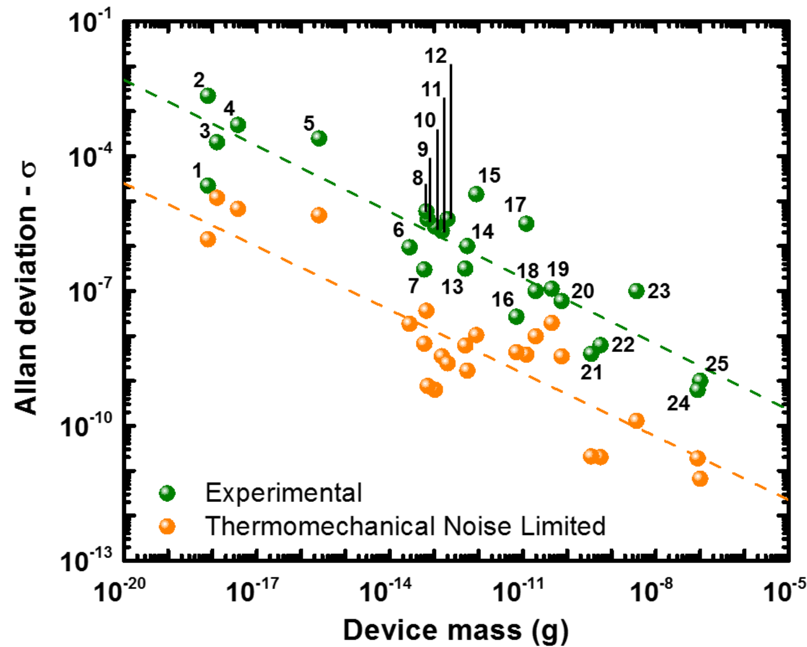

Supplementary Figure S1. Complete mapping of datapoints and references of Figure 1 in the main text.

1. Chaste, J. et al. A nanomechanical mass sensor with yoctogram resolution. Nat. Nanotechnol. 7, 301–304 (2012). *After annealing*

2. Chaste, J. et al. A nanomechanical mass sensor with yoctogram resolution. Nat. Nanotechnol. 7, 301–304 (2012). *Before annealing*

3. Jensen, K., Kim, K. & Zettl, A. An atomic-resolution nanomechanical mass sensor. Nat. Nanotechnol. 3, 533–537 (2008).

4. Chiu, H.-Y., Hung, P., Postma, H. W. C. & Bockrath, M. Atomic-Scale Mass Sensing Using Carbon Nanotube Resonators. Nano Lett. 8, 4342–4346 (2008).

5. Chen, C. et al. Performance of monolayer graphene nanomechanical resonators with electrical readout. Nat. Nanotechnol. 4, 861–867 (2009).

6. Bartsch, S. T., Rusu, A. & Ionescu, A. M. Phase-locked loop based on nanoelectromechanical resonant-body field effect transistor. Appl. Phys. Lett. 101, 153116 (2012).

7. Sansa, M., Fernández-Regúlez, M., Llobet, J., San Paulo, Á. & Pérez-Murano, F. High-sensitivity linear piezoresistive transduction for nanomechanical beam resonators. Nat. Commun. 5, (2014).

8. Hanay, M. S. et al. Single-protein nanomechanical mass spectrometry in real time. Nat. Nanotechnol. 7, 602–608 (2012). *SiN Resonator*
9. Naik, A. K., Hanay, M. S., Hiebert, W. K., Feng, X. L. & Roukes, M. L. Towards single-molecule nanomechanical mass spectrometry. Nat. Nanotechnol. 4, 445–450 (2009).
10. Ramos, D. et al. Optomechanics with Silicon Nanowires by Harnessing Confined Electromagnetic Modes. Nano Lett. 12, 932–937 (2012).
11. Feng, X. L., White, C. J., Hajimiri, A. & Roukes, M. L. A self-sustaining ultrahigh-frequency nanoelectromechanical oscillator. Nat. Nanotechnol. 3, 342–346 (2008).
12. Yang, Y. T., Callegari, C., Feng, X. L., Ekinci, K. L. & Roukes, M. L. Zeptogram-Scale Nanomechanical Mass Sensing. Nano Lett. 6, 583–586 (2006).
13. Mile, E. et al. In-plane nanoelectromechanical resonators based on silicon nanowire piezoresistive detection. Nanotechnology 21, 165504 (2010).
14. Hanay, M. S. et al. Single-protein nanomechanical mass spectrometry in real time. Nat. Nanotechnol. 7, 602–608 (2012). *Crystalline Silicon Resonator*
15. Gray, J. M., Bertness, K. A., Sanford, N. A. & Rogers, C. T. Low-frequency noise in gallium nitride nanowire mechanical resonators. Appl. Phys. Lett. 101, 233115 (2012).
16. Verd, J. et al. Monolithic CMOS MEMS Oscillator Circuit for Sensing in the Attogram Range. IEEE Electron Device Lett. 29, 146 –148 (2008).
17. Villanueva, L. G. et al. A Nanoscale Parametric Feedback Oscillator. Nano Lett. 111025132735008 (2011). doi:10.1021/nl2031162
18. Gavartin, E., Verlot, P. & Kippenberg, T. J. Stabilization of a linear nanomechanical oscillator to its thermodynamic limit. Nat. Commun. 4, (2013).
19. Verd, J. et al. Design, fabrication, and characterization of a submicroelectromechanical resonator with monolithically integrated CMOS readout circuit. J. Microelectromechanical Syst. 14, 508 – 519 (2005).
20. Fong, K. Y., Pernice, W. H. P. & Tang, H. X. Frequency and phase noise of ultrahigh Q silicon nitride nanomechanical resonators. Phys. Rev. B 85, 161410 (2012).
21. Olcum, S. et al. Weighing nanoparticles in solution at the attogram scale. Proc. Natl. Acad. Sci. 111, 1310–1315 (2014).
22. Park, K. K. et al. Capacitive micromachined ultrasonic transducer (CMUT) as a chemical sensor for DMMP detection. Sensors Actuators B Chem. 160, 1120–1127 (2011).
23. Larsen, T. et al. Ultrasensitive string-based temperature sensors. Appl. Phys. Lett. 98, 121901–121901–3 (2011).
24. Ivaldi, P. et al. 50 nm thick AlN film-based piezoelectric cantilevers for gravimetric detection. J. Micromechanics Microengineering 21, 085023 (2011).
25. Burg, T. P. et al. Weighing of biomolecules, single cells and single nanoparticles in fluid. Nature 446, 1066–9 (2007).

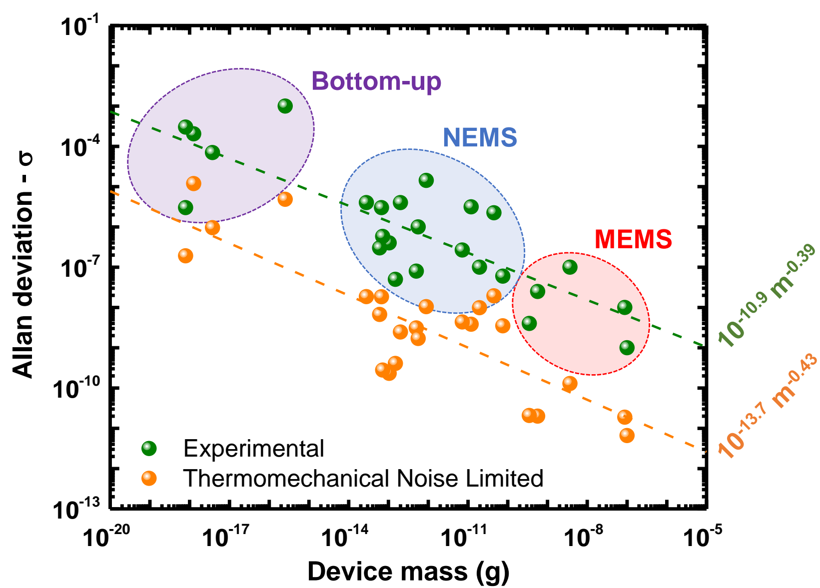

Supplementary Figure S2. Reviewed works of the literature – raw data without normalization. The main conclusion of Figure 1 in the main text remains unchanged: none of the experimental works come close to the limit set by thermomechanical noise.

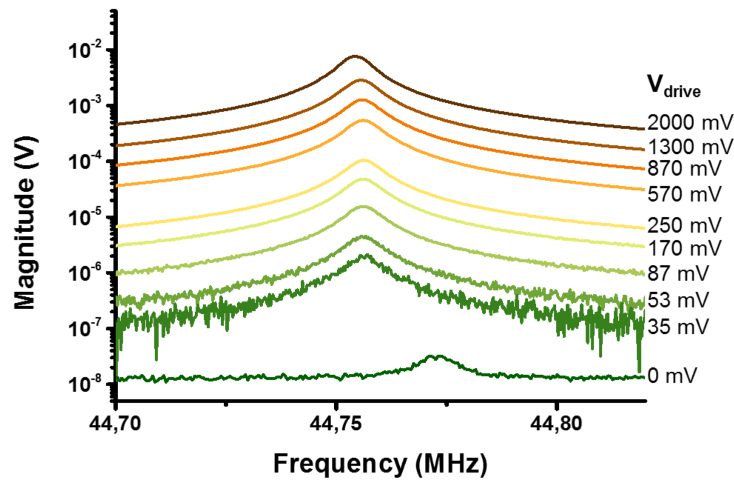

Supplementary Figure S3. Frequency response of the NEMS resonator of Figure 2b-c in the main text, for different drive voltages. The voltage values correspond to those of the Allan deviation of Figure 2c. The bias voltage through the gauges is $V_{bias} = 1.5$ V, the measurement frequency is 530 kHz and the drive voltage is applied at half the actuation frequency with no DC. The measurement at 0 mV corresponds to the measurement of the thermomechanical noise; its shift in frequency with respect to the other graphs was caused by operation condition (temperature, pressure) changes with time. The measurement at 2000 mV already shows signs of non-linearity. Using the curve at 1300 mV at the limit of non-linearity, the dynamic range of the resonator is of 107 dB for an integration time of 1s (first-order filter). By fitting the resonances we find quality factors ranging from 5950 to 6150 without a clear dependence with respect to driving voltage, suggesting the absence of non-linear damping in the resonators. We also measured the frequency response varying the speed of the sweep by two orders of magnitude. We observe no appreciable change in the quality factor, suggesting that spectral broadening due to frequency fluctuations is negligible compared to the resonator's linewidth.

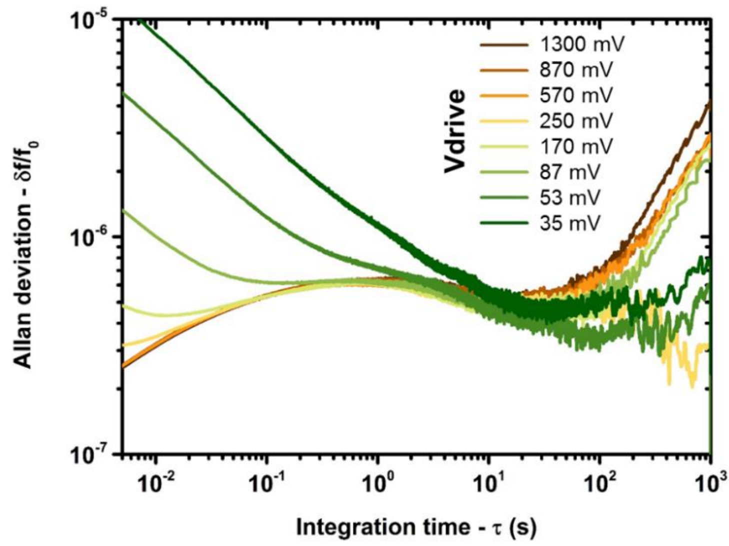

Supplementary Figure S4. Allan deviation of a monocrystalline cantilever resonator at long timescales for different drive voltages, measured during 3000s. Here the bias voltage through the gauges is V_{bias} = 1.5 V and the measurement frequency is 530 kHz. The resonator is the same as for Figure 2c in the main text. At long timescales ($\tau > 10^2$) the Allan deviation increases due to systematic drifts in the resonance frequency of the resonator.

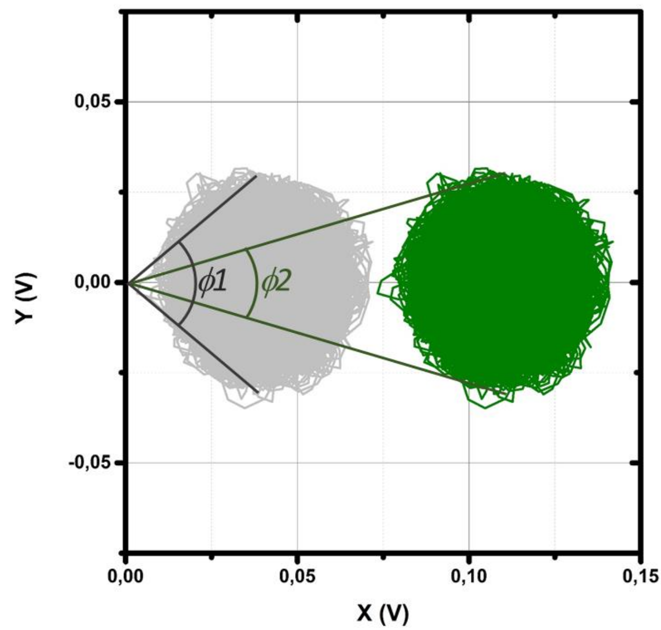

Supplementary Figure S5. Simulations of phase noise as a function of the signal-to-noise ratio (SNR), for additive white noise. White noise is added to two different signals (sinusoids) with different amplitudes (0.04 V and 0.11 V). The in-phase (X) and quadrature (Y) components of the signal are plotted. Phase fluctuation levels are denoted *ϕ1 and ϕ2*.

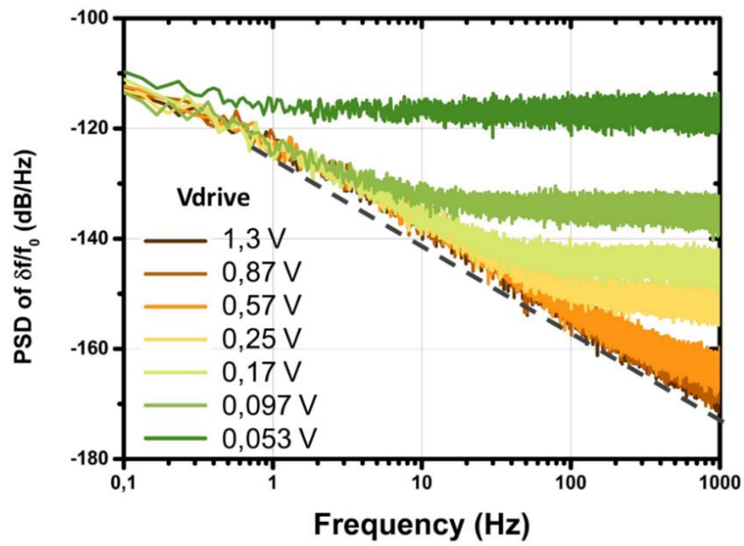

Supplementary Figure S6. Power spectral density of normalized frequency fluctuations $\delta f/f_0$. This data is obtained from phase measurements using a lock-in amplifier, and this graph is calculated from the same set of raw data than Figure 2c of the main text. The power spectral density of $\delta f/f_0$ is obtained using the Welch method. We observe the same behaviour as with the Allan deviation: for low drive voltages, white noise dominates in the major part of the spectrum. As the drive voltage is decreased, a limit appears with a 1/f main trend (dashed grey line in the figure).

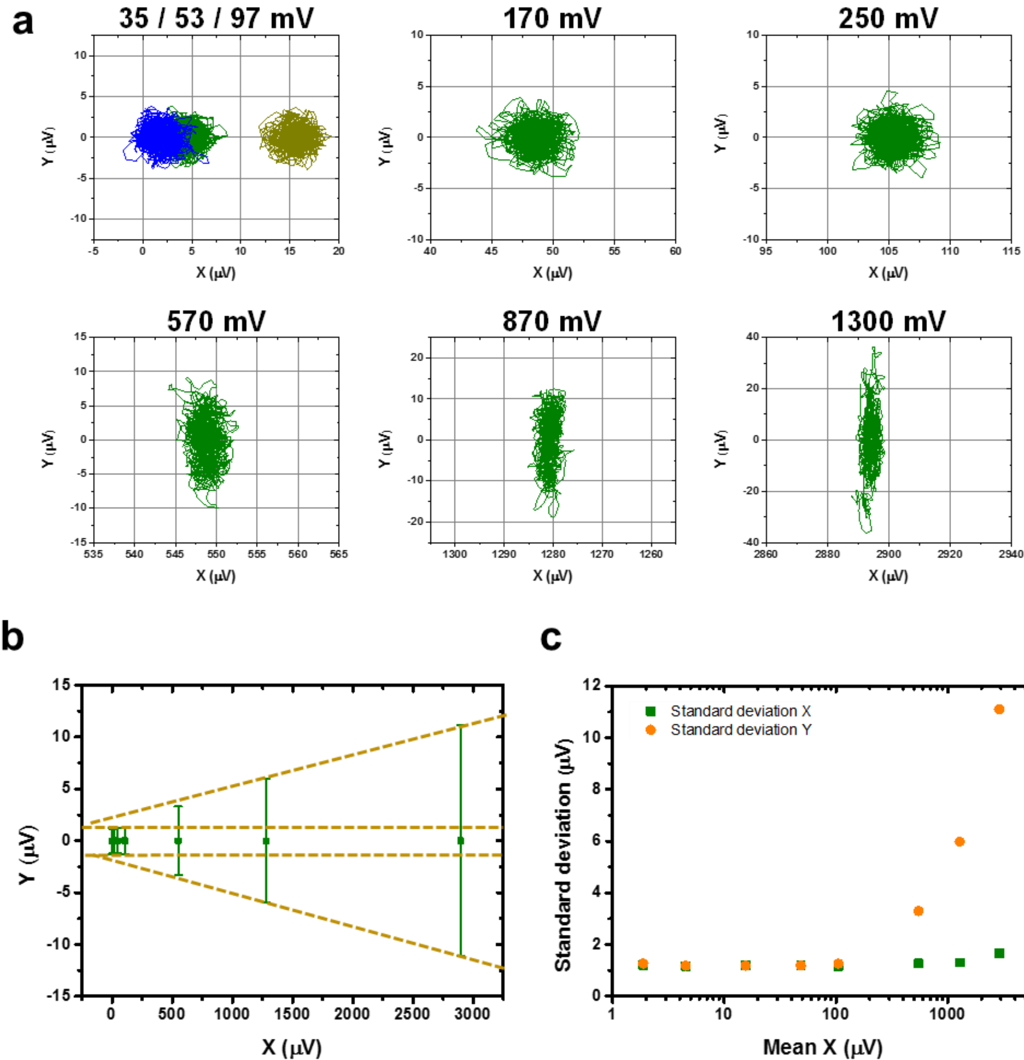

Supplementary Figure S7. Cartesian representation of samples used to calculate the phase and frequency deviations. The samples are represented by the in-phase (X) and quadrature (Y) components in µV. The graphs are built from a subset of 2000 samples taken during 75 ms, from the same data used in Figure 2c of the main text. The samples are first rotated so that the mean phase is zero (centred at X=0), and some outliers beyond 2σ from the mean of X and Y are eliminated to facilitate the visualization. **a,** Representation of the samples for different drive voltages. We observe that at low voltages the noise is white and independent of the drive voltage. At higher drive voltages (>570 mV) we observe increased phase noise (noise in Y) proportional to the drive voltage, while the amplitude noise remains constant. **b,** Representation of the mean Y value (square dot) +/- the standard deviation (bars) of the samples, as a function of the mean X value. We observe the same effect than in Figure S7a: for large driving voltages, the noise in phase (Y) is proportional to the amplitude of the signal (X). **c,** Alternative representation for b, where the standard deviations of X and Y are plotted as a function of mean X.

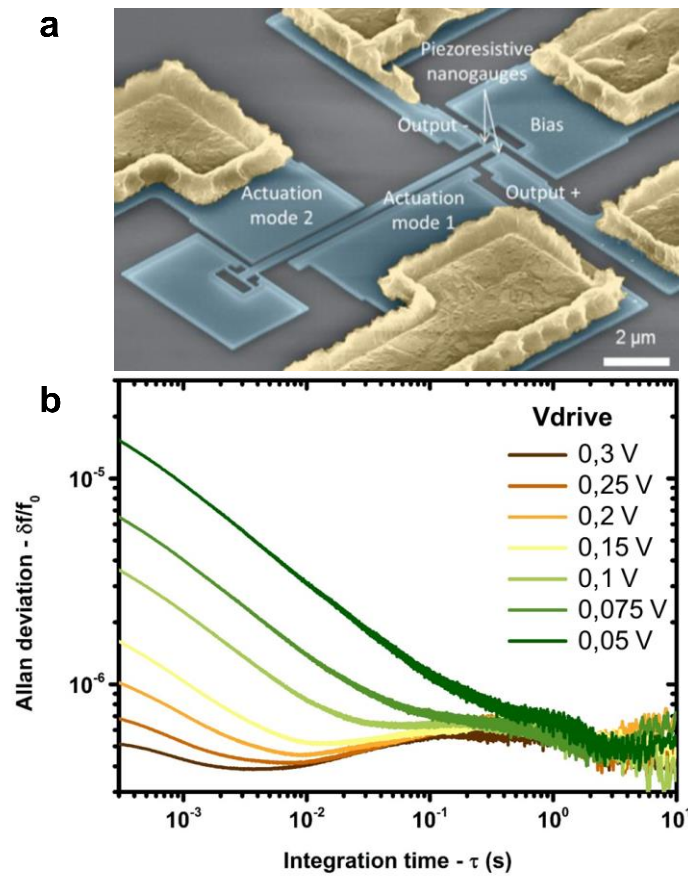

Supplementary Figure S8. Frequency stability of a clamped-clamped crystalline Si beam resonator. **a,** SEM image of the resonator, indicating the different parts of the resonator. The resonator has a length of 10 µm, and a section of 300x160 nm. The piezoresistive nanogauges have a length of 300 nm and a section of 80x160 nm. **b,** Frequency stability of the clamped-clamped beam resonator as a function of the integration time, for different drive voltages. The bias voltage is set at 1.5 V, and the measurement frequency is 530 kHz. A drive voltage of 0.3 V represents the limit of linear behaviour for this device. The frequency stability results are very similar to those of the cantilever in Figure 2c in the main text.

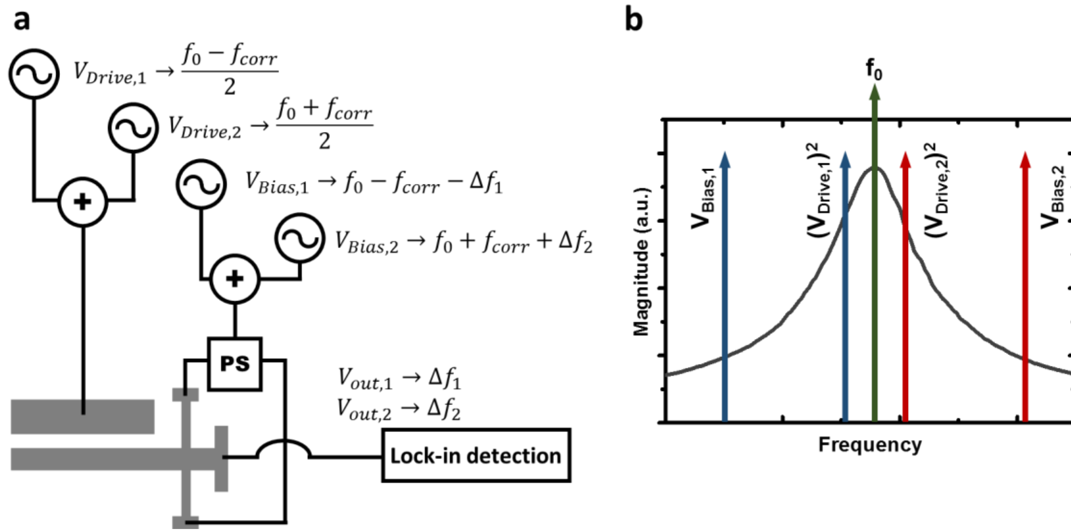

Supplementary Figure S9. Experimental set-up used to perform the correlation measurements in Figure 4 of the main text. **a,** Schematic of the set-up. It is based on the set-up described in detail in Supplementary Section 3, but each element is doubled: two different drive signals, bias signals and outputs signals are used. **b,** Representation of the different tones present in the system. The device, with resonance frequency f_0, is actuated at two different frequencies within its bandwidth by two different drive voltages, $V_{Drive,1}$ and $V_{Drive,2}$. In this case, the actuation force is at twice the frequency of the drive voltages ($F_{Drive} \alpha V_{Drive}^2$), although a drive voltage consisting of a DC plus an AC component can also be used. The two bias voltages are located out of resonance and far away from each other, to minimize interferences. To choose the bias offsets Δf_1 and Δf_2, we first perform a frequency sweeps with a single drive voltage while measuring with the two bias, and ensure that the measured responses are identical. Typical values for these parameters are: f_0 = 45 MHz, $\Delta f_1 = 300$ kHz, $\Delta f_2 = 370$ kHz and $f_{corr} = 1$ kHz.

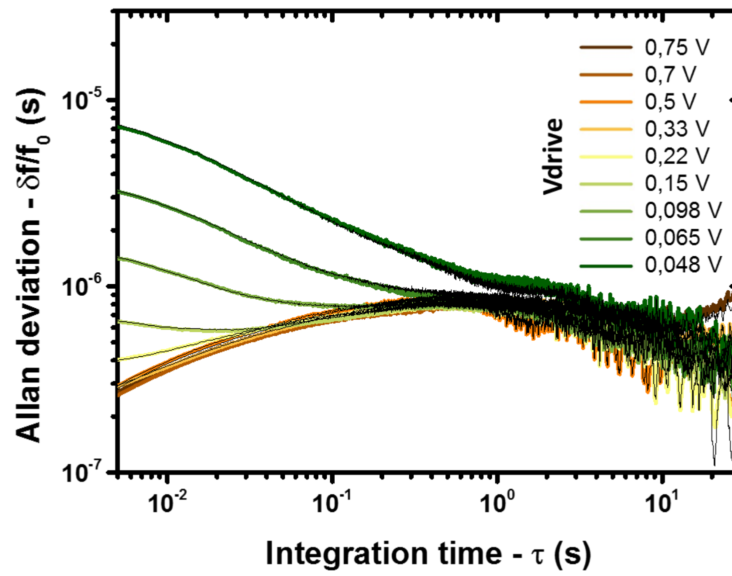

Supplementary Figure S10. Frequency stability of frequency traces measured simultaneously at two different points of the response of the resonator. The Allan deviation as a function of integration time, for different drive voltages, is calculated from the same samples as in Figure 4 in the main text. The frequency traces are measured at the resonance frequency plus and minus 1 kHz. The coloured lines represent the Allan deviation of the first frequency trace (f_0+1kHz), and the thin black lines the Allan deviation of the second one (f_0-1kHz).

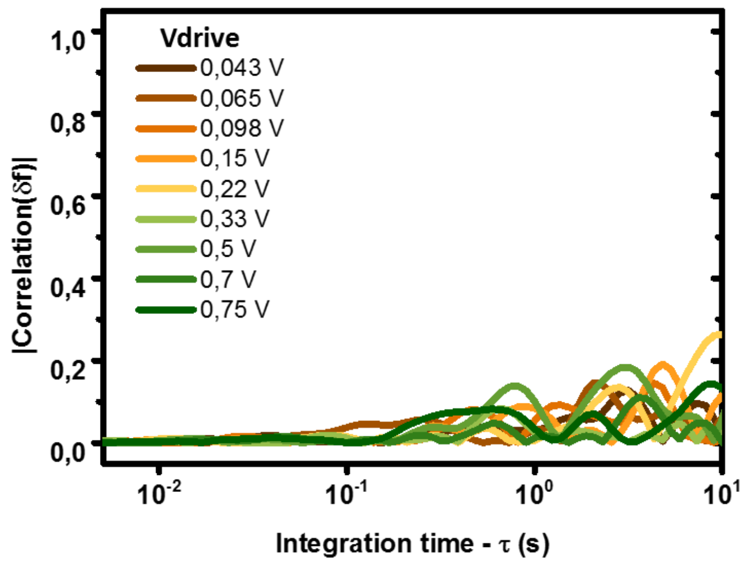

Supplementary Figure S11. Correlation of two frequency traces measured out of resonance. The measurements are performed in the same manner as in Figure 4b of the main text, and using the exact same measurement conditions (including frequency difference between the two signals) but several MHz out of resonance. In this case, the measured phase data is converted to resonance frequency as if it was obtained from the resonator, that is, using its parameters of f_0 and Q.

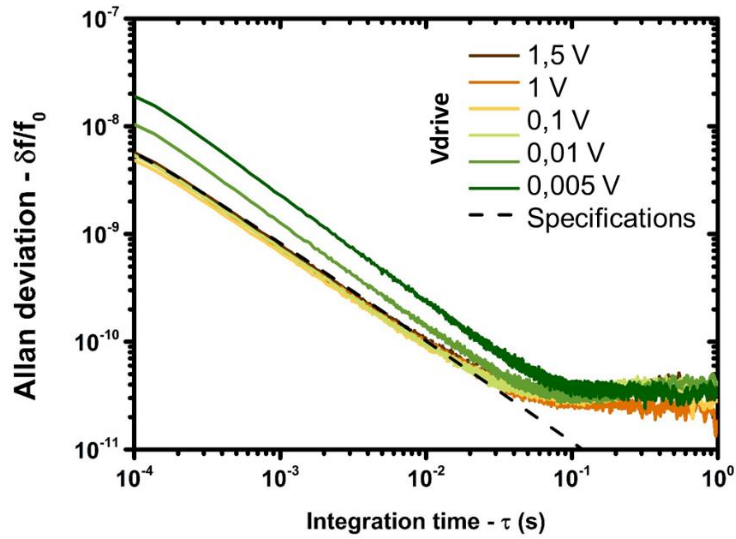

Supplementary Figure S12. Frequency stability of the RF generator which provides the drive voltage. The Allan deviation is measured as a function of the integration time, for a frequency of 40 MHz and for different amplitudes. The black dashed line represents the theoretical frequency stability according to specifications at 10 MHz, and supposing a constant f^{1} phase noise. We observe that, even in the worst case, the stability of the source is well below 10^{-7}, and therefore an order of magnitude lower than the stability results obtained with the resonator.

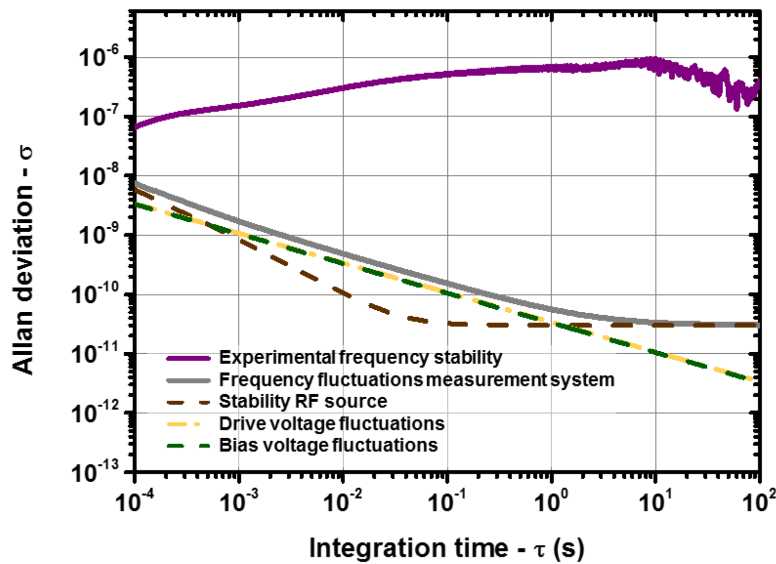

Supplementary Figure S13. Frequency fluctuations caused by the measurement system. The stability of the RF source is experimentally characterized—see Supplementary Figure **S12**—and modelled here as two regions with different slopes. The fluctuations arising from noise in the drive and bias signals are characterized as follows: first, the frequency spectrum of a cantilever resonator is measured in open loop with varying voltages of drive and bias. The results are then fitted to a Lorentzian to extract the voltage-to-resonance-frequency relationship, which may include different effects, such as the Duffing non-linearity or electrostatic stiffness tuning. This relationship is linearized around the operating point (amplitude of 1.5V, both for drive and bias). Then the frequency fluctuations are deduced from the voltage noise specified in the specifications of the RF sources ($25\,nV.Hz^{-1/2}$), white in a small bandwidth around resonance. The gray thick line represents the addition of these noise sources. The violet thick line is the open loop Allan deviation of the resonator (Figure 2c in the main text) for a drive voltage of 1.3 V and a bias voltage of 1.5 V, for comparison.

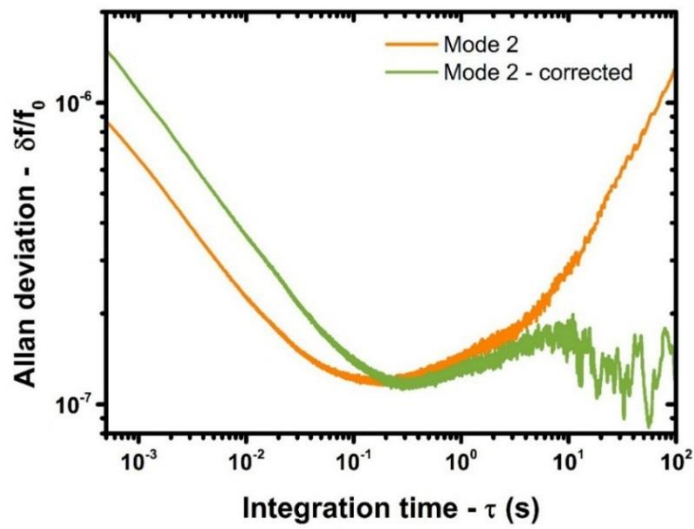

Supplementary Figure S14. Frequency stability of the second mode of a clamped-clamped beam resonator before and after the temperature correction. The results are very similar to the ones for the first mode shown in Figure 5b of the main text.

Supplementary Section 1 – Literature review: thermomechanical noise limit and normalization

In Figure 1 of the main text we compare the experimental frequency stability with the thermomechanical noise-limited stability: the thermomechanical noise spectral density in the mechanical domain (in m^2Hz^{-1}) is given by the following formula

$$S_{x,th} \approx \frac{k_B T Q}{2\pi^3 m_{eff} f_0^3} \tag{S1}$$

where m_{eff} and f_0 are the effective mass and the resonant frequency that we determined from the data available in each paper; k_B is the Boltzmann constant; T is the temperature of operation, and Q is the quality factor of the resonator. The Allan deviation was then estimated with equation (1) in the main text, expressed in the mechanical domain:

$$\sigma_{A,th} \approx \frac{1}{2Q}\frac{\sqrt{S_{x,th}}}{A_c}\frac{1}{\sqrt{2\pi\tau}} \tag{S2}$$

where τ is the integration time that is used in each paper to obtain the experimental value and A_c is the onset of non-linearity in displacement, estimated separately for each of the designs.

Given that the operation conditions were not identical throughout all works and in order to obtain data that can be better compared, we applied a normalization to account for these effects. In the calculation of thermomechanical noise-limited Allan deviation (equations (S1) and (S2)), the final result does not depend on the quality factor (Q). Indeed, if we assume the frequency stability is limited by thermomechanical noise and the resonator is driven at its onset of non-linearity (which scales like $\sqrt{\frac{1}{Q}}$), then the quality factor does not appear in equation (S2). Thus, we only rescaled the temperature and chose 300 K as the operation temperature for all cases (the rescaling factor ranges from 1 to 8.7).

For the experimental values, we assumed that the Allan deviation can be expressed as:

$$\sigma_{A,exp} \approx \frac{1}{2Q}\frac{1}{SNR}\frac{1}{\sqrt{2\pi\tau}} \tag{S2}$$

Where SNR is the signal-to-noise ratio. We also assumed the SNR depends on temperature T and to scale like $\propto T^{-1/2}$. In other words, we assumed the signal would remain constant while the noise is of thermal origin. Like above, we rescaled the temperature to 300K.

Additionally, we rescaled $\sigma_{A,exp}$ by substituting the quality factor of the resonator under study by which of the same device at 300 K and in vacuum. To obtain these values for Q we searched the literature for papers from the same groups where devices with similar frequencies, shape and material were operated under those conditions (300 K and in vacuum). In the few cases where this was not possible, we looked for other groups and similar devices operated under those conditions. The overall scaling factors for the experimental Allan deviation values ranged from 0.05 to 43 (values very different from 1 are obtained for experiments performed in air or at very low temperatures only).

Supplementary Section 2 - Fabrication of the resonators

The NEMS resonators are fabricated from 200 mm silicon-on-insulator (SOI) wafers, in a Si device layer of 160 nm and a buried oxide of 400 nm. The device Si layer is doped with boron and then annealed to obtain a homogeneous resistivity of around 9 mΩ cm. The devices (resonator, nanogauges and drive electrode) and their interconnections are defined using a hybrid e-beam/DUV lithography technique, which allows a minimum feature size of 50 nm. Then the structures are etched in the top Si layer using anisotropic reactive ion etching. A layer of AlSi is deposited in the interconnections and wire-bonding pads. Finally, the nanoresonators are released from the SiO2 layer using a vapor HF isotropic etching. The final structures are shown in Figure 2a of the main text, as well as in Supplementary Figure **S15**. The dimensions of the structure are detailed in Table S1.

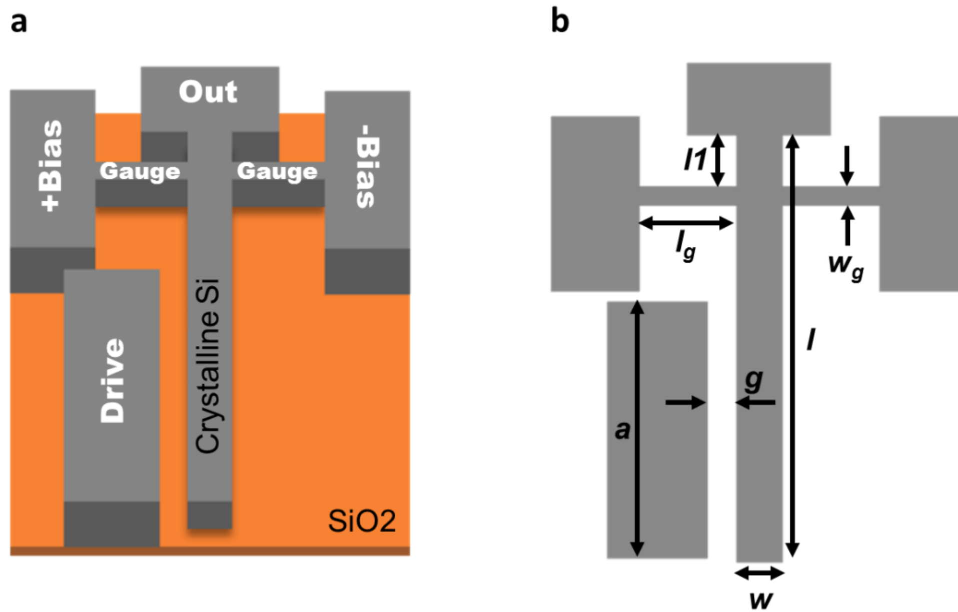

Supplementary Figure S15. Crystalline silicon NEMS resonators. **a,** Schematic of the resonator. The crystalline Si beam and nanogauges are suspended. The bias, output and drive electrodes are attached to the buried oxide layer. **b,** Dimensions of the structure, detailed in supplementary table 1.

Thickness Si layer	Length resonator l	Width resonator w	Length gauges l_g	Width gauges w_g	Gap resonator-drive g	Distance gauges-anchor $l1$
160 nm	3.2 μm	300 nm	1 μm	100 nm	150 nm	480 nm

Table S1. Dimensions of the cantilever resonator shown in Figure S15.

Supplementary Section 3 - Measurement set-up

The measurements of the NEMS resonators are performed using a downmixing set-up, shown in Supplementary Figure S16a. The resonator is electrostatically actuated, by applying a voltage to a lateral side-gate. No DC voltage is used, and the drive frequency is at half the actuation frequency (ω_0) to reduce the parasitic signal. The mechanical motion is transduced through two piezoresistive nanogauges in a differential fashion (Supplementary Figure S16b).

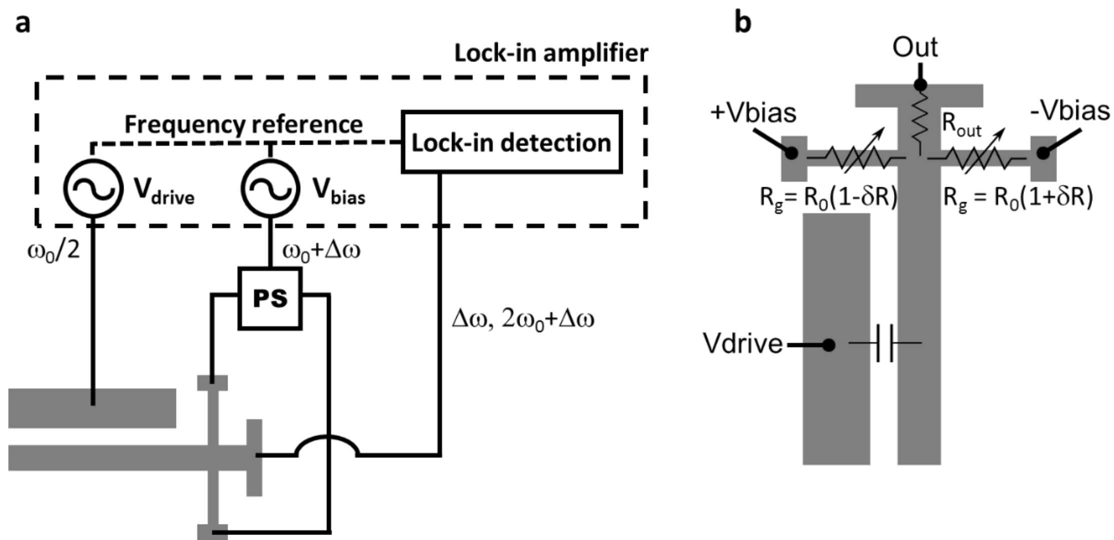

Supplementary Figure S16. Measurement method. **a,** Schematic of the down-mixing measurement set-up. As all the signals are internally generated by a single instrument, there is no need for the external reference generation branch, which is usually present in this kind of set-up. **b,** schematic of the resonator. It can be represented as two resistances at the nanogauges, and an output resistance.

The downmixing set-up allows us to measure the signal of the resonator at low frequency, in order to reduce signal loss from parasitic capacitances. In general, the gauges have a resistance $R_g = R_0(1+\delta R)$, where δR is the piezoresistive term which depends on the elongation of the gauges. When the device is at resonance at a frequency ω_0, this term becomes $\delta R=\Delta R/R_0 \cos(\omega_0 t)$. If we consider an infinite resistance of the measurement instrument, the voltage at the output of the resonator is $V_{out} = V_{Bias}\delta R$. When the bias voltage is at a frequency $\omega_0+\Delta\omega$, and the variation of the nanogauges at ω_0, an output term is mixed at low frequency $\Delta\omega$, fed into the lock-in amplifier.

Supplementary Section 4 - Effect of noise sources in the frequency stability of NEMS resonators

We study the effect of additive phase noise in the frequency stability of a NEMS resonator. The resonator is an ideal oscillator, with resonance frequency f_0. The measurement of the resonance frequency is performed by measuring the phase fluctuations of a downmixed signal. However, the fact that the measured signal is at low frequency does not affect the stability results. In general, the frequency stability of a NEMS resonator measured with a bandwidth B can be defined from the spectral noise density in frequency $S_f(f)$, which has units of Hz^2/Hz [1]:

$$\langle \delta f \rangle = \left[\int_{f_0 - \pi B}^{f_0 + \pi B} S_f(f)\, df \right]^{1/2} \tag{S3}$$

As the resonance frequency is indirectly measured from the phase fluctuations, we study the case where the stability is dominated from additive noise in the phase signal. In this case, the spectral density of frequency noise can be defined from the spectral density of phase fluctuations:

$$S_f(f) = \frac{S_\varphi(f)}{(\partial\varphi/\partial f)^2} \tag{S4}$$

The relationship between phase and frequency is obtained from the transfer function of the resonator. In general, the measurement of the phase is performed at the resonance frequency and the phase fluctuations are small. Under these conditions, $\partial\varphi/\partial f \cong 2Q/f_0$ if the resonator's response is Lorentzian. It is not the case anymore in the presence of, for example, frequency fluctuations. The associated spectral broadening causes an error in the observed quality factor. In our case, typical resonance frequency and quality factor of our devices are 45MHz and 6000 respectively. This translates into a width at half maximum of about 7.5kHz. For the long time scales used in our measurements, we measure a typical frequency stability limited by frequency fluctuations of about 10^{-7}, inducing a spectral broadening around 5Hz. This ratio (of more than 3 orders of magnitude) is independent on the quality factor, meaning for these time scales, the error associated with the way the quality factor is measured is negligible. This is further confirmed by the fact that no change in Q could be observed when different sweeping speeds were used to plot the frequency response (See Supplementary Figure S3). On the other hand,

---

[1] K. L. Ekinci, Y. T. Yang, and M. L. Roukes, "Ultimate limits to inertial mass sensing based upon nanoelectromechanical systems," J. Appl. Phys., vol. 95, no. 5, pp. 2682–2689, Mar. 2004.

the employed measurement scheme is insensitive to frequency fluctuations with correlation times smaller than the decay rate of the resonator. Should such fluctuations significantly contribute to the observed quality factor, an error would be made by using the perturbative treatment leading to the expression of $\partial\varphi/\partial f$. This would all the more show how strong the effect of frequency noise can be for such resonators.

Besides measuring the quality factor by the linewidth of the driven resonator, we also measure the linewidth of the Brownian motion, as well as the ring-down time of the resonator (see Figure S17). All three measurements are very consistent within measurement precision. It should also be noted that the amplitude of the measured Brownian peak does not change with the driving signal, as shown in the white noise regime in Figure 2c of the main text.

As importantly, a large error in the measurement of Q would only shift upwards or downwards all curves in Figure 2 of the main text, both theoretical and experimental, by the same ratio. Hence all our conclusions would still hold.

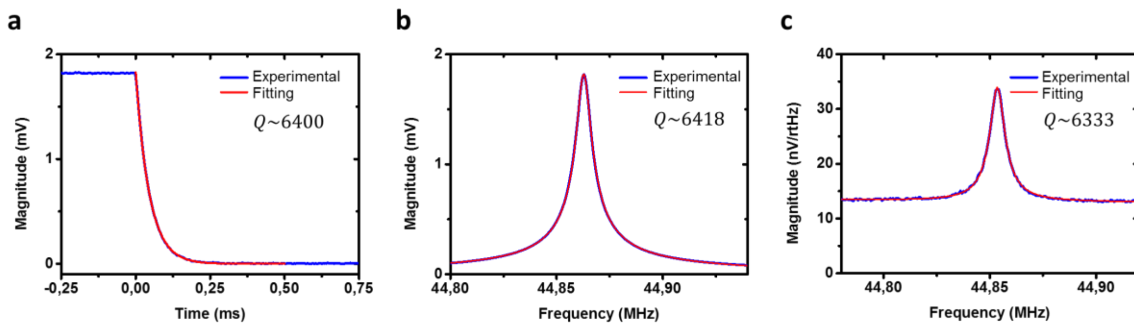

Supplementary Figure S17. Measurement of the quality factor measured using different methods. **a,** Measurement of the quality factor using the ring-down method. The measurement is performed using the set-up of Supplementary Figure **S16**. Both output and drive signals were monitored simultaneously. The resonator is driven at resonance and the drive voltage is set to 0 at time t=0 on the graph. The output signal is recorded with a time constant of 1.5 μs, roughly 100 times smaller than the response time of the resonator. The magnitude of the undriven signal is fitted to $Ae^{-\frac{f_0}{2Q}}$, where the only unknown is the quality factor Q. With this method, we find Q=6400. **b,** Linewidth measurement of the same driven resonator yielding Q=6418. **c,** Linewidth measurement of the thermomechanical peak yielding Q=6330.

The phase deviations of a noisy oscillator signal can be defined in terms of the signal to noise ratio of the measurement [2]. Therefore the spectral density of phase fluctuations can be defined as:

[2] W. P. Robins, "Phase Noise in Signal Sources," *Electronics and Power*, vol. 30. Peter Peregrinus Ltd., IET, p. 82, 1984.

$$S_{\varphi}(f) = \frac{N_v(f)}{S_v^2} \tag{S5}$$

Where $N_v(f)$ is the spectral density of voltage fluctuations in V^2/Hz, and S_v is the amplitude of the measured signal in volts. Then in general the frequency noise caused by an additive phase noise in the measurement can be expressed as:

$$\langle \delta f_{phase} \rangle = \frac{f_0}{2Q}\frac{1}{S_v}\left[\int_{f_0-B/2}^{f_0+B/2} N_v(f)\, df\right]^{1/2} \tag{S6}$$

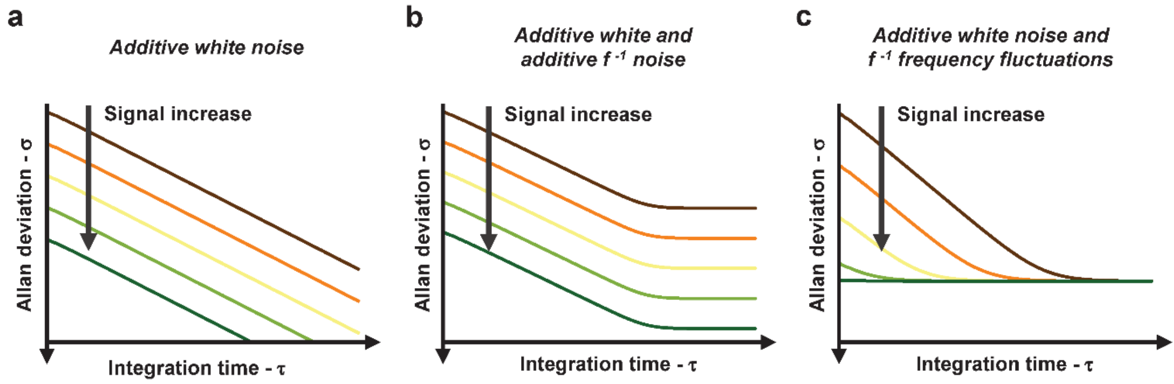

Supplementary Figure S18. (Figure 3 of the main text, reproduced here for convenience) Effect of different noise sources on the frequency stability as a function of the integration time τ, and for different signal levels. **a,** Additive white noise, manifesting itself as phase noise. It presents a constant slope of $\tau^{-1/2}$. The stability improves with increasing signal level. **b,** Combination of additive white and f^{-1} noises. For low integration times it presents a slope of $\tau^{-1/2}$, which becomes τ^0 when the f^{-1} noise dominates at large integration times. The stability improves with increasing signal level in the whole time range. **c,** Combination of additive white noise with f^{-1} frequency-fluctuations. For low integration times it presents a slope of $\tau^{-1/2}$, which becomes τ^0 when the f^{-1} frequency noise dominates. Moreover, the stability due to frequency fluctuations is insensitive to the signal level: therefore, an increase in the signal has an effect only when additive noise dominates.

One of the most common noise in the detection is white noise, for example noise in the detection or Johnson noise. In this case $N_v(f) = N_{0,white}^2$, (where $N_{0,white}$ has units of $V \times Hz^{-1/2}$) then the resonance frequency noise is:

$$\langle \delta f_{phase,white} \rangle = \frac{f_0}{2Q}\frac{N_{0,white}}{S_v}B^{1/2} \tag{S7}$$

This expression is used to fit the frequency stability in Supplementary Figure **S18**a. Another common noise source is f^{-1} noise, which can be originated from Hooge noise in the resistances, or detection noise at low frequencies. In this case, $N_v(f) = N_{0,f^{-1}}^2/f$. In the case that the

measurement bandwidth is much smaller than the resonance frequency ($B \ll f_0$), the integral of the expression is:

$$\int_{f_0-B/2}^{f_0+B/2} N_{0,f^{-1}}^2/f\, df = N_{0,f^{-1}}^2 \frac{ln(f_0 + B/2)}{ln(f_0 - B/2)} \cong N_{0,f^{-1}}^2 \quad \text{(S8)}$$

Then the frequency noise is

$$\langle \delta f_{phase,f^{-1}} \rangle = \frac{f_0}{2Q} \frac{N_{0,f^{-1}}}{S_v} \quad \text{(S9)}$$

Finally, in general the frequency stability is affected by different noise sources:

$$\langle \delta f \rangle = \left[\int_{f_0-\pi B}^{f_0+\pi B} \left(S_{f1}(f) + S_{f2}(f) + \cdots \right) df \right]^{1/2} \quad \text{(S10)}$$

Supplementary Figure **S18**b shows the Allan deviation in the case of additive white noise (equation S7) combined with f^{-1}noise equation (S9).

In the situation studied in the main text, the resonator is affected by additive phase noise and frequency fluctuations $S_{f_0}(f)$.

$$\langle \delta f_{phase,frequency} \rangle = \left[\frac{f_0}{2Q} \frac{1}{S_v} \int_{f_0-B/2}^{f_0+B/2} N_v(f)\, df + \int_{f_0-B/2}^{f_0+B/2} S_{f_0}(f)\, df \right]^{1/2} \quad \text{(S11)}$$

This situation is plotted in Supplementary Figure **S18**c, where we show the special case of white additive phase noise and an f^{-1}frequency fluctuation noise:

$$\langle \delta f_{Fig.3c} \rangle = \left[\left(\frac{f_0}{2Q} \frac{N_{0,white}}{S_v} \right)^2 B + \delta f_A \right]^{1/2} \quad \text{(S12)}$$

Supplementary Section 5 - Temperature compensation experiments

For this experiment, doubly-clamped beam resonators are placed in a liquid nitrogen cryostat with temperature control (these resonators display the same frequency fluctuations than cantilevers but their first and second mode frequencies are closer than cantilevers). The temperature coefficients TC_{f1} and TC_{f2} are obtained by measuring the frequency response of the resonator at different temperatures, and fitting it to a Lorentzian to obtain the resonance frequency. The temperature is controlled by a resistive heater located at the base of the chip containing the resonator, and measured by a temperature sensor located close to the heater. The measurements are performed several times, sweeping the temperature up or down, to ensure that the observed dependence arises from temperature changes instead of time drifts. The temperature dependencies of these two frequencies are linear in a wide range around room temperature (Figure 5a in the main text), and are close to expectations (TC_{f1}=-28 $ppm\ °C^{-1}$ and TC_{f2}=-36 $ppm\ °C^{-1}$ for the first and second modes respectively.

The frequency traces $f_1(t)$ and $f_2(t)$ of the two first modes are recorded over some period of time (typically 300s). The Allan deviations of both modes in this measurement show similar features (Supplementary Figure **S19**). The instantaneous temperature variation (actually its spatial average within the resonator) is given by $\Delta T = \frac{(f_2 - \bar{f_2})}{TCf_2}$ where $\bar{f_2}$ is the sample mean of $f_2(t)$. The temperature-compensated frequency of mode 1 is then given by $f_{1,C}(t) = f_1(t) - TC_{f1}\Delta T(t)$, and its Allan deviation can be computed.

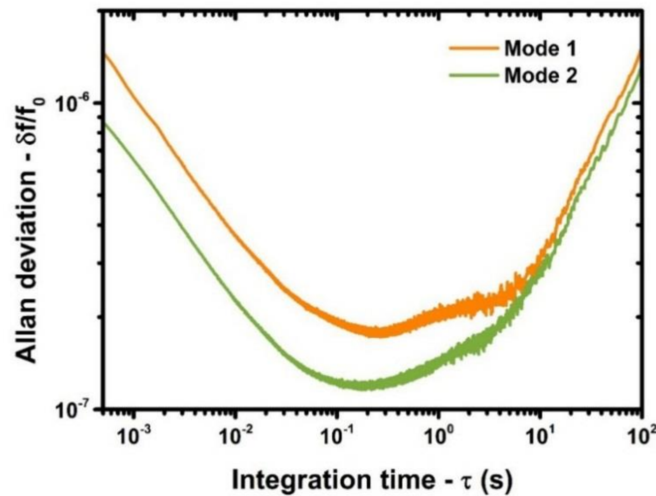

Supplementary Figure S19. Frequency stability of a clamped-clamped beam resonator, for the first two modes of resonance. In this case, the frequency stability of both modes is measured simultaneously. The stability of both modes has a very similar shape, with three different regimes like for the first mode only.

Figure 5b in the main text shows the comparison between the uncompensated and temperature-compensated frequency stabilities of mode 1. Unsurprisingly, frequency stability is significantly improved by our temperature compensation technique in the long-term regime (integration times $\tau > 10^1$ s), dominated by temperature drifts. In the frequency fluctuations regime ($10^{-1}\ s < \tau < 10^1\ s$) however, we observe only a slight improvement of the stability, by a very small extent compared to the level added by the frequency fluctuations. Correcting the temperature dependence of the second mode using the first one as a temperature probe provides the same result (Supplementary Figure S14). Our correction assumes a uniform temperature change within the resonator, ignoring the effect of potential local temperature changes (due to, for instance, particles impinging on the device): indeed, the small heat capacitance of our resonators yield a thermal time constant of around few nanoseconds, much smaller than the measurement time. Of course, this technique would – partially—cancel out any source inducing correlated fluctuations of the two modes, and we attribute the slight improvement of stability in the intermediate regime to this effect. This is similar to the work in [3], who used a feedback loop to compensate for the fluctuations of one mode by monitoring the fluctuations of another mode. The compensation was not based on measured temperature

[3] Gavartin, E., Verlot, P. & Kippenberg, T. J. Stabilization of a linear nanomechanical oscillator to its thermodynamic limit. Nat Commun 4, (2013).

sensitivities of frequency but on a feedback corrector experimentally chosen to cancel as much as possible the fluctuations. The fact that a large part of the fluctuations were compensated for indicates the presence in their system of a fluctuation source affecting both modes, like temperature variations for example. By contrast, our results suggest that temperature fluctuations cannot account for the frequency fluctuations in our silicon resonators.

Supplementary Section 6 - Sources of frequency fluctuations

Adsorption-desorption

The adsorption-desorption noise is quantified following the method described in references [4], [5]. In our case, we consider measurements at room temperature (T=300K), with a pressure of 5×10^{-5} mbar and a contamination by nitrogen. With this parameters we calculate the ratio of adsorption of molecules per area:

$$r_a = \frac{2}{5}\frac{P}{\sqrt{mk_BT}}s \tag{S13}$$

Where P is the pressure, m is the mass of the adsorbing molecules, s is the sticking ratio (here we suppose that it is 0.1). We suppose 1 adsorption site each $0.25\ nm^2$. The desorption attempt rate per site is:

$$r_d = v_d exp\left(-\frac{E_b}{k_BT}\right) \tag{S14}$$

Where v_d is the desorption attempt rate (10^{13}, in the order of the vibrational frequency of a diatomic molecule) and E_b the binding energy, which is 10 kcal/mol in our case. The parameter values used for the calculation of adsorption/desorption ratios (s, E_b and v_d) are based on Ref [5], which shows an experimental validation of these formulae in the case of Xe atoms.

Supposing a measurement time τ_A much larger than the correlation time of the adsorption/desorption process ($\tau_r = 1/(r_a + r_d)$), the frequency fluctuations arising from this process are:

$$\sigma_a(\tau_a) = \frac{1}{2\sqrt{3}}\sigma_{occ}\sqrt{N_a}\left(\frac{m}{M}\right)\left(\frac{\tau_r}{\tau_a}\right)^{1/2} \tag{S15}$$

Where $\sigma_{occ} = \sqrt{r_a r_d}/(r_a + r_d)$ is the surface occupation deviation, N_A is the number of adsorption sites in the resonator, τ_a the integration time of the measurement and M is the mass of the resonator. The Allan deviation obtained in this way is more than 4.5 orders of magnitude

---

[4] A. N. Cleland and M. L. Roukes, “Noise processes in nanomechanical resonators,” J. Appl. Phys., vol. 92, no. 5, pp. 2758–2769, Sep. 2002.
[5] Y. T. Yang, C. Callegari, X. L. Feng, and M. L. Roukes, “Surface Adsorbate Fluctuations and Noise in Nanoelectromechanical Systems,” Nano Lett., vol. 11, no. 4, pp. 1753–1759, 2011.

lower than the experimental results. Even though a number of parameters in these calculations are estimations, even a large error in these would not account for this difference.

Surface diffusion

Molecules attached to the resonator can also diffuse through its surface. This effect changes the mass distribution of the resonator, and therefore causes resonance frequency fluctuations. Under certain conditions (resonator subjected to a flow of molecules at low temperature) this effect has been shown to be the dominating source of frequency fluctuations [5], when the mean occupation of adsorbing sites of the resonator is large. In our case, however, the occupation ratio of adsorbing sites is found to be very small, due to the fact the experiments are carried out at low pressure and room temperature. Following the development in [5], the Allan deviation when the time constant of the diffusion process is much smaller than the measurement time ($\tau_D \ll \tau_A$) can be expressed as

$$\sigma_d(\tau_a) \approx 0{,}83\sqrt{N}\left(\frac{m}{M}\right)\left(\frac{\tau_D}{\tau_a}\right)^{1/4} \tag{S16}$$

where N is the number of atoms in the surface and τ_D is the time constant of the diffusion process. For a measurement time much larger than the diffusion time ($\tau_A \ll \tau_D$) this expression becomes:

$$\sigma_d(\tau_a) \approx 0{,}51\sqrt{N}\left(\frac{m}{M}\right)\left(\frac{\tau_a}{\tau_D}\right)^{1/2} \tag{S17}$$

Here we suppose a diffusion time $\tau_D$in the order of 0.1 s, in the same order of magnitude of Xe atoms diffusing in a NEMS resonator. Measurement times used in our experiments are chosen in a range starting from well below the diffusion time up to values well above. In order to obtain a crude estimation of the surface diffusion fluctuations at intermediate values, we assume that the inverse of the total Allan deviation can be described as the addition of the inverse of equations (S16) and (S17). Again, there is a huge difference between the theoretical values of the frequency fluctuations due to surface diffusion and the experimental results (close to 13 orders of magnitude). Even huge errors in parameter values would not account for this difference in magnitude.

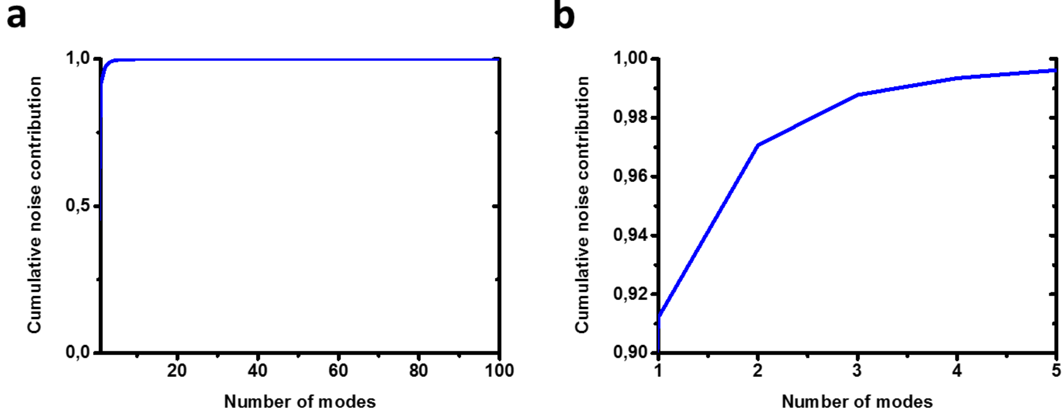

Supplementary Figure S20. Calculated cumulative contribution of higher modes to the frequency fluctuations of the first mode through non-linear mode-coupling. Higher modes vibrate due to thermomechanical noise. The graph shows the cumulative noise for the first 100 modes. **b,** Detail of figure **a** showing only the first 5 modes. The contribution of the first mode to itself is due to the Duffing non-linearity. The first two modes account for 97% of the total frequency fluctuations.

Non-linear mode-coupling

The resonance frequency of one mode of a resonator depends on the amplitude of motion of the same mode (via the Duffing non-linearity) and of the other modes (non-linear mode coupling). Even though this effect is especially relevant at large amplitudes of motion, some works have described frequency fluctuations arising from thermomechanical noise coupled through the Duffing non-linearity or non-linear mode coupling. The relationship between the change of resonance frequency of mode N (Δf_N) as a function of the amplitude of motion of mode M (A_M) can be derived from Euler Bernoulli theory, which includes tension. The tension depends on transverse displacement and this is the origin of non-linear mode coupling[6], [7]:

$$\frac{\Delta f_N}{f_N} = S_{MN} A_M^2 \tag{S18}$$

Where S_{MN} is the coupling term. There clearly is a cut-off in the order of modes perturbing the frequency of one mode; we calculated the coupling coefficient between the first mode and the first 100 modes of the resonator using the same method as in reference [7] and Ref. 51 of the main text, and computed the frequency fluctuations arising from thermomechanical noise of

[6] Westra, H. J. R., Poot, M., van der Zant, H. S. J. & Venstra, W. J. Nonlinear Modal Interactions in Clamped-Clamped Mechanical Resonators. Phys. Rev. Lett. 105, 117205 (2010).

[7] Matheny, M. H., Villanueva, L. G., Karabalin, R. B., Sader, J. E. & Roukes, M. L. Nonlinear Mode-Coupling in Nanomechanical Systems. Nano Lett. (2013).

each one of these modes. We found that the combined noise of modes 1 and 2 already account for 97% of the total frequency fluctuations caused by the first 100 modes of the resonator (Supplementary Figure **S20**). The frequency of mode 1 is perturbed by its amplitude fluctuation due to the Duffing non-linearity.

We measured the coupling coefficients and the thermomechanical noise of the first two modes, in order to estimate the frequency fluctuations caused by non-linear mode coupling. In the particular case of the Duffing non-linearity S_{11}, we measure the dependence of the resonance frequency of the resonator on its amplitude of motion (Supplementary Figure ***S21.***), when driven at resonance with a drive voltage of 1.5 V.

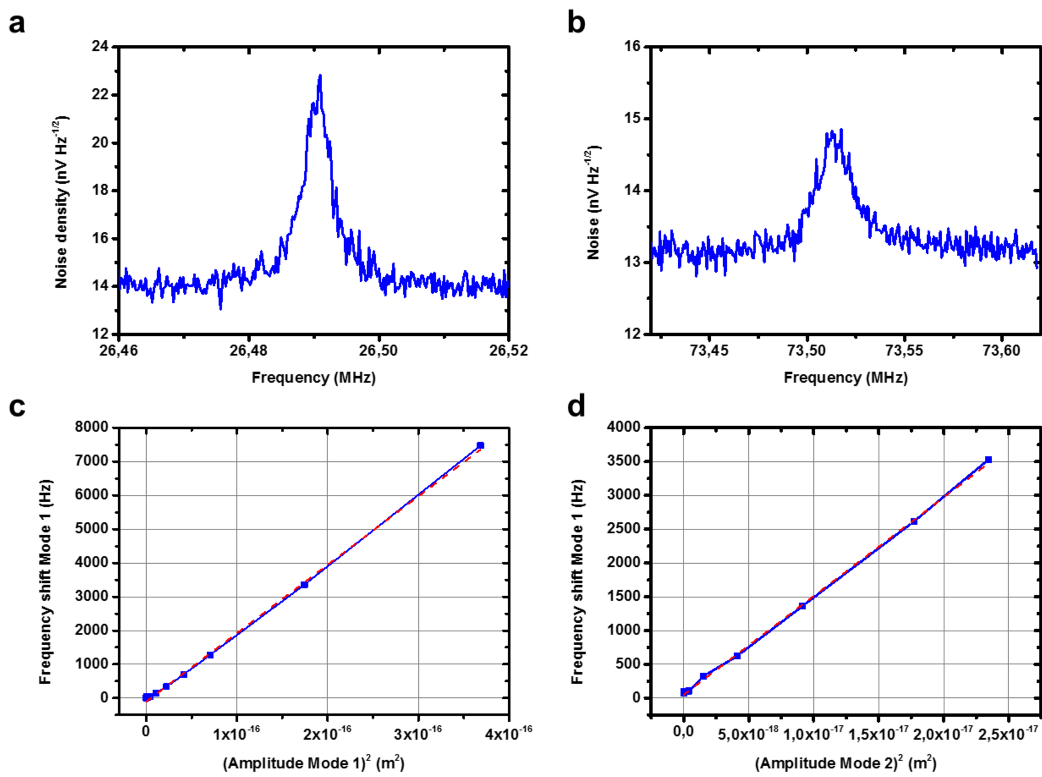

Supplementary Figure S21. Frequency fluctuations arising from non-linear mode-coupling in a clamped-clamped resonator. Thermomechanical noise measurements of the first two modes of the resonator allow us to characterize the sensitivity of the measurement set-up. **a,** Thermomechanical noise of mode 1. The sensitivity of the measurement set-up is $3.2 \times 10^4\ V/m$. **b,** Thermomechanical noise of mode 2. The sensitivity of the set-up is $8.8 \times 10^4\ V/m$. **c,** Resonance frequency of mode 1 as a function of its oscillation amplitude. The curve is obtained by operating the resonator in closed loop with a PID while changing the driving voltage. The phase error is continuously monitored to ensure a correct operation of the PID. The amplitude to voltage dependence is calculated to fit $\frac{\Delta f_1}{f_1} = 7.6 \times 10^{11} A_1^2$ (red dashed line). **d,** Resonance frequency of mode 1 as a function of the oscillation amplitude of mode 2. The curve is obtained by monitoring the resonance frequency of mode 1 with a PID, with a small amplitude of motion. At the same time, we perform frequency sweeps to monitor

the frequency response of mode 2. The points in the figure are taken from the peak of the frequency response obtained with these sweeps. The amplitude to voltage dependence is fitted to $\frac{\Delta f_1}{f_1} = 5.5 \times 10^{12} A_2^2$ (red dashed line). In Figures **c-d**, for high amplitude values, the resonator is in a highly nonlinear regime, where electrostatic tuning is negligible compared to the Duffing nonlinearity arising from the stiffening of the resonator.